Batteries & Supercaps

Articles
doi.org/10.1002/batt.202000137

Chemistry
Europe
European Chemical
Societies Publishing

Controlling at Elevated Temperature the Sodium Intercalation Capacity and Rate Capability of $P3$-Na$_{2/3}$Ni$_{1/2}$Mn$_{1/2}$O$_2$ through the Selective Substitution of Nickel with Magnesium

Mariya Kalapsazova,[a] Pavel Markov,[a] Krassimir Kostov,[a] Ekaterina Zhecheva,[a] Diana Nihtianova,[a, b] and Radostina Stoyanova*[a]

The integration of sodium-ion batteries into large-scale energy storage systems will become feasible in the case when their performance becomes less sensitive towards ambient temperature. Herein, we demonstrate the elaboration of the oxide-based electrode material with an optimized layered structure and composition that is designed to work at elevated temperatures. Through selective substitution of Mg^{2+} ions for Ni^{2+} in the three-layered oxide, $P3$-Na$_{2/3}$Ni$_{1/2}$Mn$_{1/2}$O$_2$, the oxidation state of Ni ions, the cationic distribution in the layers, the sodium intercalation capacity, and the rate capability is manipulated.

The electrochemical behavior of $P3$-Na$_{2/3}$Ni$_{1/3}$Mg$_{1/6}$Mn$_{1/2}$O$_2$ is discussed on the basis of ex situ diffraction as well as microscopic and spectroscopic methods in terms of redox activity of the lattice oxygen, the reversible transfer of Mg^{2+} and Ni^{2+} ions between layers during Na$^+$ intercalation, thermal stability of cycled electrodes, and surface reactivity of the layered oxide towards the ionic liquid (IL) electrolyte. At 40°C, the rate capability of the oxide is improved upon using an IL electrolyte rather than the carbonate-based electrolyte.

1. Introduction

Searching for energy storage technology for large-scale applications, there is a strong need to design electrode materials exhibiting performance that is less sensitive towards the ambient temperature. Metal substitution in transition metal oxides is a valid approach for improving the performance of electrode materials for lithium- and sodium-ion batteries, allowing tailoring the electrochemical properties by modeling of the electronic and crystalline structures.[1] The most intriguing system is layered lithium-transition metal oxides (Li$_{1+x}$TM$_{1-x}$O$_2$), where the main constituent ions (i.e., TM=Co, Ni and Mn) are replaced by electrochemically inactive ions (such as Mg^{2+}, B^{3+}, Al^{3+}, etc.).[2–4] Among the electrochemically inactive dopants, the Mg^{2+} ions display an ionic radius close to the one of Li$^+$ ions (0.72 versus 0.076 0.76 Å), thus allowing for a stabilization of the layered structure by occupying the interlayer slabs like in the case of Li$^+$.[5–7] The stable crystal structure, obtained by doping with Mg^{2+} ions, resulted into an enhanced thermal stability, cycling and rate capabilities of the

layered oxides, as well as in their improved microstructure and electrode kinetics.[8,9] Irrespective of the different ionic radii of Mg^{2+} and Na$^+$, the same metal substitution approach has been applied to the design of sodium transition metal analogues (Na$_{1-x}$TMO$_2$).[10–13] The specific feature of the Mg-substituted oxides (vs. the pristine ones) is their very high intercalation capacity (i.e. about 220 mAh/g), which results from the unlocking of the oxygen redox activity in addition to the conventional TM redox processes.[14] The simultaneous redox activity of oxygen and TM ions has been first reported for lithium-excess oxides (Li$_{1+x}$TM$_{1-x}$O$_2$) with a three-layer stacking[15] (O3-type structure, according to Delmas notation[16]). Several models of the redox activity have been proposed involving the transformation of oxygen anion (O^{2-}) into peroxide (O$_2^{q-}$) with shortened O—O distance,[17] the stabilization of holes in the oxygen 2p orbitals,[18] the development of a specific local environment around the oxygen atoms in disordered oxide systems,[19] and specific oxygen chemical bonds.[11] Although the redox activity of Li$_{1+x}$TM$_{1-x}$O$_2$ has been intensively investigated, the work on the Mg-substitution on Na$_x$TMO$_2$ is rare.[10,11]

The main representatives of Mg-substituted systems are Mn-rich oxides with a composition of Na$_{2/3}$[Mg$_{0.28}$Mn$_{0.72}$]O$_2$ and Na$_{2/3}$[Mg$_{1/3}$Mn$_{2/3}$]O$_2$ having two and three layer stacking, respectively ($P2$ and $P3$-type).[10,14] The effect of Mg^{2+} ions is related to a suppression of the phase transition occurring during the complete extraction of Na$^+$ at high voltages.[14] Recently, sodium nickel manganese oxides ($P3$-Na$_{0.5}$[Ni$_{0.25}$Mn$_{0.75}$]O$_2$, $P3$-Na$_{0.67}$[Ni$_{0.2}$Mn$_{0.8}$]O$_2$), which do not contain any Mg^{2+} ions, have been shown to display high intercalation capacity, too.[20,21] It is considered that the changes in Ni 3d-O

[a] Dr. M. Kalapsazova, Dr. P. Markov, Dr. K. Kostov, Prof. E. Zhecheva,
     Dr. D. Nihtianova, Prof. R. Stoyanova
     Institute of General and Inorganic Chemistry
     Bulgarian Academy of Sciences
     1113 Sofia, Bulgaria
     E-mail: radstoy@svr.igic.bas.bg
[b] Dr. D. Nihtianova
     Institute of Mineralogy and Crystallography
     Bulgarian Academy of Sciences
     Sofia, Bulgaria

2p hybridization during charging at high potentials play an important role in activation of the redox oxygen reaction.[21] Also, above 4.0 V the full extraction of Na^+ out of $P3$-$Na_{0.5}$ $[Ni_{0.25}Mn_{0.75}]O_2$ has been shown to proceed due to the intercalation of counter anion from electrolyte (such as ClO_4^-), accompanied by an activation of oxygen redox reaction (O^{2-} ↔O^-).[20] The Mg-doping of sodium nickel manganese oxides possessing a $P2$-structure ($P2$-$Na_{2/3}[Ni_{1/3-x}Mg_xMn_{2/3}]O_2$) has been found out to improve their cycling stability due to the suppression of the high-voltage structure transformation from $P2$ into $O2$.[13,22,23] Moreover, the Mg-doping provokes an enhancement in the Na^+ mobility by 2 orders of magnitude in comparison with the parent oxide $P2$-$Na_{0.67}Ni_{0.3}Mn_{0.7}O_2$.[22] The main drawback of oxides operating with simultaneous TM and oxygen redox reactions is their poor reversibility. In addition, Mg- and Ni-containing oxides display different cycling stability and rate capability.[10,13,14,20–23] Therefore, the question is what specific effects Mg^{2+} and Ni^{2+} ions have on the intercalation capacity of mixed Mg–Ni oxides, as well as what type of layers stacking ($P3$ or $P2$-type) contributes to the redox mechanism. Understanding the structural and electrochemical properties of Mg-substituted oxides could meet the challenge of designing electrode materials operating at high temperatures – an important step for large-scale utilization of sodium-ion batteries.

Herein we explore the selective substitution of Ni^{2+} ions by Mg^{2+} in a $Na_{2/3}Ni_{1/2}Mn_{1/2}O_2$ with a three layer stacking and their effects on the sodium intercalation capacity and rate capability at elevated temperature. The sodium nickel-manganese oxides, $Na_{2/3}Ni_{1/2}Mn_{1/2}O_2$, are selected since they assume a structure, which is flexible enough to acquire a three layer stacking (i.e., $P3$-type) and to adopt a large trigonal superstructure with a "flower-like" cationic order inside the layers (i.e., $2\sqrt{3} \times 2\sqrt{3}$), as well as Ni and Mn ions are stabilized in oxidation states of $+2/+3$ and $+4$, respectively.[24,25] In comparison with the $P3$-oxide, the $P2$-oxide that also contains nickel and manganese ($Na_{2/3}Ni_{1/3}Mn_{2/3}O_2$) exhibits a superstructure with reduced lattice parameters.[26] In addition, the $P3$-phase $Na_xNi_{0.5}Mn_{0.5}O_2$ is prone to accumulate much more sodium than the P2-phase ($0.5 <= x <= 1.2$ versus $0.5 <= x <= 0.8$), which is of importance for practical application.[27] Because of structural and compositional peculiarities, the $P3$-oxide displays improved cycling stability within an extended potential range than that of the $P2$-phase.[24,27] Taking into account the advantages of the flexibility of the $P3$-type of structure and the positive effect of Mg^{2+} ions on the energy storage we are developed oxide with optimized structure and composition, displaying a good performance at elevated temperatures.

Through the selective replacement of Ni ions by Mg^{2+} ions, the oxidation state of Ni ions, the cationic distribution in the layers and the sodium intercalation capacity can be manipulated. This approach differs from the one used so far, in which the Jahn-Teller Mn^{3+} ions are replaced by electrochemically inactive ions such as Zn^{2+} in order to enhance the structural stability and electrode performance.[28] The chemical composition, crystalline structure, cationic distribution, and the oxidation states of the TM ions and the thermal properties of Mg-

substituted oxides $Na_{2/3}Ni_{1/2-x}Mg_xMn_{1/2}O_2$ are analyzed via complementary diffraction and spectroscopic methods. The sodium intercalation capacity of $P3$-$Na_{2/3}Ni_{1/2-x}Mg_xMn_{1/2}O_2$ is determined using galvanostatic measurements in half-sodium cells with two types of sodium electrolytes: conventional carbonate-based electrolyte and ionic liquid electrolyte (IL). Ex-situ XRD, TEM and EPR experiments are undertaken in order to gain insight into effects of Mg-dopants on the storage performance of $P3$-$Na_{2/3}Ni_{1/2-x}Mg_xMn_{1/2}O_2$. The surface of electrodes after cell charging and discharging at 20 and 40 °C is assessed by applying ex-situ XPS analysis.

2. Results and Discussion

2.1. Structure of P3-Na$_{2/3}$Ni$_{1/2-x}$Mg$_x$Mn$_{1/2}$O$_2$

Mg-substituted oxides $P3$-$Na_{2/3}Ni_{1/2-x}Mg_xMn_{1/2}O_2$ ($x=0.04$, 0.08, 0.16) were obtained by thermal decomposition of the freeze-dried acetate precursors. The stoichiometry of the materials was confirmed by ICP analysis and the nominal vs measured content of Na, Mn, Ni and Mg is listed in Table S1 (SI).

The experimental and simulated XRD patterns of the Mg-substituted oxides can be indexed by a structural model, comprising a main phase with a three-layer stacking ($R3\ m$ space group) and traces of a NiO-like cubic phase (Fm-$3\ m$ space group, Figure S1, SI). The same model has been used to index the XRD pattern of NNM.[24] According to Rietveld refinement analysis, the relative content of the NiO-like phase is lower than 1% with no dependence on the nominal Mg content.

The crystal structure of the NNM oxide consists of TM layers, between which the Na^+ ions are located adopting the prismatic coordination, i.e., $P3$-structure. By increasing the degree of substitution of Ni^{2+} ions by Mg^{2+} ions, the $P3$-structure is preserved and the unit cell volume shows a tendency to enlarge (Table 1). This is consistent with a preferential substitution of Ni^{2+} by Mg^{2+} ions, having a slightly higher ionic radius (0.70 Å versus 0.72 Å). For the sake of comparison, the ionic radius of low-spin Ni^{3+} ion is 0.56 Å.[29] The preferential replacement of nickel by magnesium is also supported by the EPR study of synthesized $P3$-$Na_{2/3}Ni_{1/2-x}Mg_xMn_{1/2}O_2$ compounds (Figure S2, SI). At a threshold concen-

Table 1. Lattice parameters for $P3$-$Na_{2/3}Ni_{1/2-x}Mg_xMn_{1/2}O_2$ powder as synthesized and recovered from NM-16 electrodes after numerous cycling between 2.0 and 4.3 V in NaFSI- and NaPF$_6$-based electrolytes.

x	Electrolyte/temperature/state of charge	A [Å]	c [Å]	V [Å³]
0.0	Pristine	2.8867	16.7692	121.01
0.04	Pristine	2.8865	16.7723	121.02
0.08	Pristine	2.8871	16.7753	121.09
0.016	Pristine	2.8889	16.7789	121.27
0.16	NaFSI/20 °C/stop at 4.3 V	2.8763	16.9178	121.21
0.16	NaFSI/20 °C/stop at 2.0 V	2.8927	16.7735	121.55
0.16	NaFSI/40 °C/stop at 2.0 V	2.8896	16.7940	121.43
0.16	NaPF$_6$/20 °C/stop at 2.0 V	2.8956	16.8055	122.03
0.16	NaPF$_6$/40 °C/stop at 2.0 V	2.8979	16.7969	122.16

tration of $x = 1/6$, the charge compensation is attained by presence of Mg^{2+}, Ni^{3+} and Mn^{4+} ions only.

The Mg^{2+} ions affect also the distribution of Ni and Mn ions inside the TM layer (Figure 1). The TEM analysis of the NM-16 indicates a formation of nano-sized particles that are bonded into micrometric aggregates (Figure 1). The SAED is indexed by a layered structure having lattice parameters identical with those determined based on XRD analysis (Figure 1). The nano-sized particles show well resolved lattice fringes corresponding to an interlayer space of 0.56 nm (Figure 1). Close inspection of SAED and HR-TEM indicates that there is no lattice super-structure, which is typical of the unsubstituted $Na_{2/3}Ni_{1/2}Mn_{1/2}O_2$ oxide (Figure S3).[24] This fact reveals that the Mg^{2+} doping disrupts the Ni and Mn ordering inside in the TM layer of parent $Na_{2/3}Ni_{1/2}Mn_{1/2}O_2$. The lack of cationic ordering is an interesting finding considering that Mg^{2+} doping of Na_xMnO_2 with two layer stacking (P2-type) results in a $\sqrt{3}a$ x $\sqrt{3}a$-type super-lattice ordering inside the TM layers, while the layers arrange to give columns of Mg ions.[27,30] It is worth mentioning that $P3$-$Na_{2/3}Ni_{1/2}Mn_{1/2}O_2$ displays a larger super-lattice ordering in comparison with that of the P2-phase: $2\sqrt{3}$ x $2\sqrt{3}a$ versus $\sqrt{3}a$ x $\sqrt{3}a$, respectively.[24,30] The comparison suggests that the cationic ordering inside the TM layer depends both on the ionic radii and on the chemical properties of Ni and Mg ions.

2.2. Electrochemical Properties of $P3$-$Na_{2/3}Ni_{1/3}Mg_{1/6}Mn_{1/2}O_2$

The progressive replacement of Ni^{2+} with Mg^{2+} in $P3$-$Na_{2/3}Ni_{1/2-x}Mg_xMn_{1/2}O_2$ culminates at $x = 0.16$, i.e., the composition at which only the Ni^{3+} ions exist according to the overall material's charge balance. This composition is actually examined as an electrode material, because the high oxidation sate of Ni ions contributes to an oxygen redox activity via strong Ni 3d-O 2p hybridization,[21] as well as Ni^{3+} can either take or release one electron resulting into either $Ni^{3+} \rightarrow Ni^{2+}$ or $Ni^{3+} \rightarrow Ni^{4+}$ redox processes, respectively. Since the sodium content is equal to 0.67 (i.e., less than 1 mole per formula unit), both of

the above redox processes can be balanced by either insertion or extraction of Na^+ ions. The capability of $P3$-$Na_{2/3}Ni_{1/3}Mg_{1/6}Mn_{1/2}O_2$ to intercalate Na^+ ions is demonstrated in Figure 2. Below 3.0 V, NM-16 inserts 0.37 mole Na^+ (corresponding to a specific capacity of 102 mAh/g) mostly along a voltage plateau of 1.95 V. This fact reveals that the Mg-substituted oxide $Na_{2/3}Ni_{1/3}Mg_{1/6}Mn_{1/2}O_2$ reaches the theoretical amount of one mole of Na^+ per formula unit after the first sodiation step (i.e., $Na_{2/3+0.37}Ni_{1/3}Mg_{1/6}Mn_{1/2}O_2$). A similar behavior is also shown by the unsubstituted oxide, $Na_{2/3}Ni_{1/2}Mn_{1/2}O_2$, but at a lower voltage and to a minor extent.[24] In fact, the plateau's voltage decreases from 1.93 to 1.75 V for x going from 0.16 to 0 (Figure S4, SI). The amount of inserted Na^+ reaches a 0.3 mole, which matches with a fraction of Ni^{3+} appeared in non-substituted $Na_{2/3}Ni_{1/2}Mn_{1/2}O_2$ (i.e. 1/6 Ni^{2+} and 1/3 Ni^{3+}, respectively).

The reverse charging reaction proceeds along four well-developed plateaus and it delivers a specific capacity of 293 mAh/g, which corresponds to an extraction of 1.08 mole of Na^+ out of the sodiated oxide $Na_{2/3+0.37}Ni_{1/3}Mg_{1/6}Mn_{1/2}O_2$. This value is higher in comparison with the structural formula, where the maximum of Na^+ occupancy in the interlayer sites is limited to 1.0 mole. The higher value than 1.0 mole implies that partial electrolyte decomposition above 4.0 V. It is of importance that the inserted Na^+ content is higher in comparison with the theoretical capacity of the Mg-substituted oxide. Assuming that Mg^{2+} ions are electro-chemically inactive and blocking an equal amount of Na^+ in the chemical formula (i.e. $Na_{1/6}Ni_{1/3}Mg_{1/6}Mn_{1/2}O_2$), the total amount of Na^+ available for extraction should be 0.84 mole. Thus, to justify the measured capacity, the activation of the redox activity of lattice oxygen in $P3$-$Na_{2/3}Ni_{1/3}Mg_{1/6}Mn_{1/2}O_2$ must be invoked. The redox activity of lattice oxygen has already been found out in sodium nickel-manganese oxides such as $P3$-$Na_{0.5}Ni_{0.25}Mn_{0.75}O_2$ and $P3$-$Na_{0.67}Ni_{0.2}Mn_{0.8}O_2$.[19,20] The new finding herein is that Mg^{2+} ions induce an increase in the potentials, when sodium intercalation takes place (Table 2), somehow resembling the effect of Al^{3+} dopant on the potential of $LiTMO_2$ compounds upon Li^+ intercalation.[31,32] In case of layered $LiCoO_2$, it has experimentally and theoretically been demonstrated that the substitution of Al^{3+} for Co^{3+} enhances the covalency of the M–O bond, thus causing the increase in the intercalation potential and the
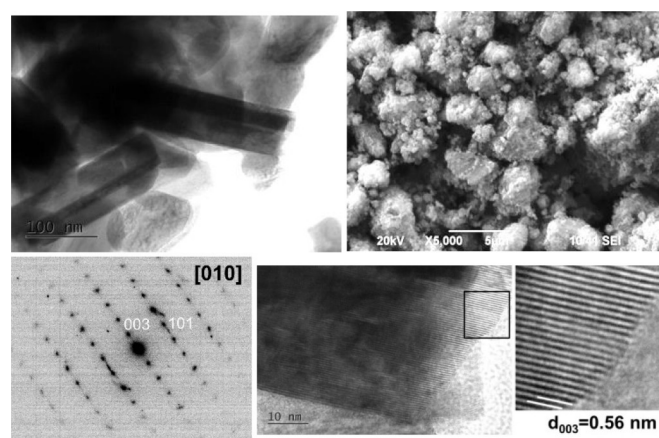

Figure 1. TEM bright field micrograph (top, left), SEM image (top, right), SAED of NM-16 (bottom, left) and their HRTEM images corresponding to interlayer space of $d_{003} = 0.56$ nm (bottom, right).
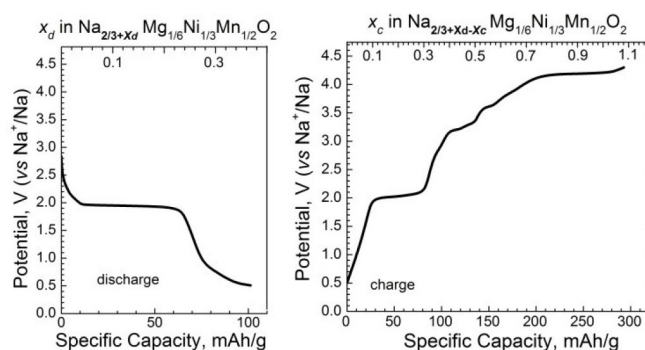

Figure 2. First discharging (left) and charging (right) curve for $Na_{2/3}Ni_{1/3}Mg_{1/6}Mn_{1/2}O_2$ in a sodium half-cell. For the sake of convenience, both the specific capacity and the mole of Na^+ intercalated are given.

Table 2. Potential of Na^+ insertion in and extraction out of $Na_{2/3}Ni_{1/2}Mn_{1/2}O_2$ and $Na_{2/3}Ni_{1/3}Mg_{1/6}Mn_{1/2}O_2$ determined from the first discharging and consecutive charging (see Figure S4).

Charge [V]	NNM	2.25	3.20	3.28	3.63	4.20
	NM-16	2.02	3.24	3.33	3.64	4.22
Discharge [V]	NNM	1.75	3.19	3.27	3.57	4.12
	NM-16	1.95	3.22	3.32	_[a]	_[a]

[a] These peaks are broadened and they are hardly distinguished.

decrease in the intercalation capacity.[31,32] A similar phenomenon have been observed for the polyanionic compounds with a NASICON-type structure, when simultaneous presence of Ca and Fe ions induced an increase in the potential of the redox couple Ti^{4+}/Ti^{3+}.[33] The specific role of Mg^{2+} dopants in $P3$-$Na_{2/3}Ni_{1/2-x}Mg_xMn_{1/2}O_2$ is to enhance the intercalation potential without causing any significant changes in the intercalation capacity (Figure S4, SI).

Starting the test in charging mode, i.e., first de-sodiating $P3$-$Na_{2/3}Ni_{1/2-x}Mg_xMn_{1/2}O_2$, the voltage profile shows three plateaus at 3.2, 3.6 and 4.2 V (Figure 3 and Figure S5). These are the same voltage plateaus observed starting the test in discharging mode (compare Figure 2 and Figure S5). After the first charge, NM-16 delivers a capacity of 137 mAh/g corresponding to the extraction of 0.51 mol of Na^+ (Figure 3 and Figure S5). It is noticeable that this capacity is again higher than the expected one. According to structural and EPR data, Mg^{2+} ions substitute the Ni^{2+} in $P3$-$Na_{2/3}Ni_{1/2-x}Mg_xMn_{1/2}O_2$ culminating, at a threshold concentration of $x=1/6$, to a charge compensation with Ni^{3+} only. This indicates that only 1/3 of Na^+ can be extracted out of $P3$-$Na_{2/3}Ni_{1/3}Mg_{1/6}Mn_{1/2}O_2$ at the expense of oxidation of Ni^{3+} to Ni^{4+}. The observed higher capacity points, once again, to the important role of the lattice oxygen during the sodium extraction. However, at potentials higher than 4.0 V, the instability of the carbonate-based electrolyte should be taken into account, which could lead to an additional increase in the capacity.[34] To analyze the possible electrolyte decomposition at potentials higher than 4.0 V, Figure S6 shows the charging/discharging curves for the unsubstituted oxide NNM, where the upper voltage limit progressively increases from 4.2 up to 4.5 V, keeping the lower voltage limit down to 2.0 V. As one could expect, the charge capacity associated with a high-voltage plateau increases progressively upon extension of the upper voltage limit. Contrary to the charging capacity, the discharging capacity shows a higher value at an intermediate voltage limit of 4.3 V. This experiment indicates that the possible decomposition of the $NaPF_6$-based electrolyte can be disregarded up to 4.3 V, while above 4.3 V there is significant electrolyte decomposition. For this reason, all the experiments are carried out up to 4.3 V.

Because $P3$-$Na_{2/3}Ni_{1/2-x}Mg_xMn_{1/2}O_2$ is designed as a cathode material, only the reaction proceeding above 2.0 V is of practical interest. Thus, in this work the electrochemical performance of NM-16 is studied within the voltage window of 2.0–4.3 V, where three voltage plateaus are observed (i.e. at 3.2, 3.6 and 4.2 V, see also Figure S5). Figure 3 shows the charging/discharging curves relative to the 1st and 20th cycle of NNM and NM-16 at 0.1 C and 0.5 C. At low C-rate, i.e. 0.1 C, the 1st charging curve of NM-16 shows some plateau-like features at 3.2, 3.6 and 4.2 V, while the discharging curve shows a slope-like profile with only one well-distinguished plateau at 3.2 V (Figure 3). This fact is in contrast with the NNM electrode, where both charging and discharging curves display three voltage plateaus (Figure 3). In accordance with our previous studies,[24] the extraction of the first half mole of Na^+ at 3.2 and 3.6 V is concomitant with a monoclinic distortion of the $P3$-type of structure. The second half mole of Na^+ is extracted during the voltage plateau at 4.2 V, corresponding to a reverse switching to an undistorted $P3$-structure having rather larger interlayer space.[24]

For NM-16, the charging plateau at 4.2 V displays a strong C-rate dependence. Upon increasing the C rate from 0.1 up to 0.5 C, the high voltage charge plateau shortens dramatically, while the two plateaus at 3.2 and 3.6 V are unaffected (Figure 3). As a result of this, the charge capacity decreases at a faster C-rate. Interestingly, the discharging curve profile and the corresponding discharging capacity do not undergo any significant changes, when increasing the C rate from 0.1 up to 0.5. The different rate dependence for the charging and discharging curves indicates that the reaction at 4.2 V comprises, at least, two competitive processes, i.e. one highly reversible, while the other one is irreversible and kinetically limited.

The unsubstituted oxide NNM displays also rate dependence of the 4.2 V charge plateau, but to lower extent than that of the Mg-substituted oxide (Figure 3). This trend, however, is reversed upon cycling (Figure 3). Moreover, the discharge plateau at 4.2 V becomes shorter with an increase of the C-rate, as well as upon cycling (Figure 3). This leads to a more significant reduction in the discharge capacity than that in case of the NM-16 (Figure 3). The C-rate induced changes in the
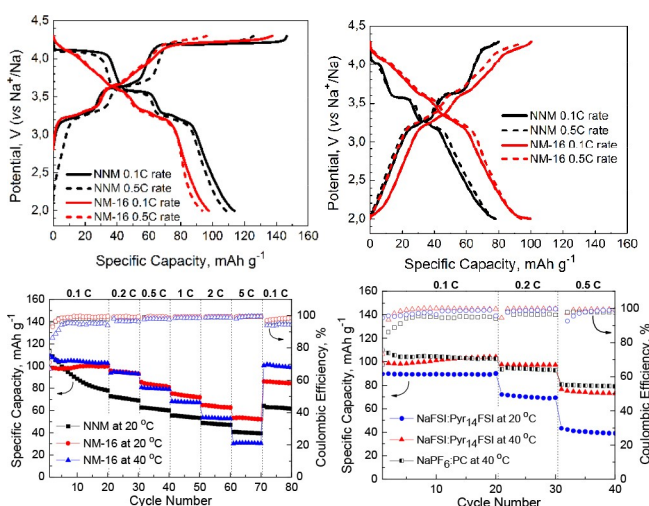

Figure 3. Charging/discharging curves of NNM and NM-16 recorded during the 1st cycle (left) and the 20th cycle (right) at 0.1 and 0.5 rate in $NaPF_6$-PC electrolyte. (bottom, left) Rate capability tests for NNM (at 20 °C) and NM-16 (at 20 and 40 °C) electrodes using the $NaPF_6$-PC electrolyte; (bottom, right) Rate capability tests for NM-16 electrodes employing the NaFSI-Pyr_{14}FSI electrolyte (at 20 and 40 °C).

charging/discharging curve profile at 4.2 V suppose an irreversible and kinetically limited reaction at 4.2 V to prevail in case of unsubstituted NNM oxide. On the contrary, for the Mg-substituted oxide the irreversible reaction is suppressed at the expense of the reversible one. This could tentatively be related to specific role of oxygen lattice during electrochemical intercalation of Na^+ in Mg-substituted oxide and will be discussed below.

The differences in the reaction mechanism at 4.2 V determine the improved rate capability of the Mg-substituted oxides in comparison with the unsubstituted one (Figure 3). At the lowest C-rate, the unsubstituted oxide displays a higher capacity, which diminishes quickly during cycling. On the contrary, the specific capacity of the Mg-substituted oxide is lower, but the cycling stability is excellent. At faster C-rates, NM-16 delivers higher capacity in comparison with that of unsubstituted NNM. The better rate performance of the Mg-substituted oxide is a consequence of the suppression of kinetically limited reaction at 4.2 V. In addition, the cycling stability of the Mg-substituted oxide is also impressive compared to that of the parent oxide (Figure S7).

The operating temperature is another parameter affecting the charging/discharging curves of the NM-16 electrode as it is shown in the dQ/dV plots (Figure 4, see also Figure S8). By increasing the temperature from 20 °C to 40 °C, the charging plateau at 4.2 V splits into two components at 4.04 and 4.22 V, while the overall charging capacity increases from 137 to 164 mAh/g (Figure S8). This corroborates the hypothesis about the proceeding of two competitive reactions along the high voltage plateau. The change in the charging curve profile takes place without any significant alteration in the discharging curve profile. However, the discharging capacity increases from 98 up to 110 mAh/g upon the temperature increase (Figure 3). After the first cycle, the next charging and discharging profiles

measured at 20 and 40 °C look likes similar, but the specific capacity at 40 °C remains higher (Figure 3).

Figure 3 also illustrates the rate capability of the pristine and Mg-substituted oxides in dependence on the operating temperature. The comparison shows that, at 20 °C, the rate capability of NM-16 exceeds that of NNM. The operating temperature strongly affects the rate capability of the Mg-substituted oxide: at 20 °C, NM-16 displays a better rate capability than that at 40 °C. It is worth mentioning that the operating temperature does not affect the Coulombic efficiency especially at the higher rates.

The temperature dependence of the rate capability in case of the Mg-substituted oxide is an interesting observation. There are several factors influencing the rate capability of cathodes, such as thermal stability and conductivity of electrolyte, cathode-electrolyte inter-phase, wettability, etc.). For the poly-anionic compounds, it has been found out that the volatility and instability of the organic electrolyte (i.e. 1 M $NaClO_4$ in EC/DEC) are responsible for the decrease in the high-rate performance of $NaFePO_4$ at temperatures above 50 °C.[35] For the sodium-transition metal oxides (i.e. $NaNi_{1/3}Fe_{1/3}Mn_{1/3}O_2$), the cycling at 45 °C has been demonstrated to accelerate the decomposition of $NaPF_6$ concomitant with decomposition and dissolving of the cathode–electrolyte interphase.[36] Concerning the well-known layered $LiCoO_2$, the rate capability has been shown to decrease at discharge rates greater than 2 C.[37] This unusual behavior has been explained in terms of conductivity in the liquid phase and contact area between active particles and the electrolyte (i.e. wettability).[37] Regarding electrochemical behavior of NM-16, the conductivity of $NaPF_6$-PC electrolyte is known to increase with temperature, as well as the evaporation of the organic electrolyte becomes significant at 60 °C.[38,39] Therefore, based on above mentioned data, one could suppose that the worse rate capability of NM-16 at 40 °C is dictated both by low thermal stability of $NaPF_6$-PC and by the wetting of the electrode by the electrolyte. This deserves further studies, which are in progress.

To rationalize the effect of the electrolyte, the carbonate-based electrolyte was replaced by an ionic liquid-(IL) based electrolyte, i.e., NaFSI in $Pyr_{14}FSI$ (1:9 molar ratio). It should be noticed that the IL-based electrolyte exhibits lower conductivity (4.5 mS/cm *versus* 7.98 mS/cm at 20 °C) and higher viscosity (74 mPa.s *versus* 7 mPa.s at 20 °C) in comparison with $NaPF_6$-PC.[40–42] The charging/discharging curves at 20 °C and 40 °C of NM-16 electrodes in the NaFSI-Pyr_{14}FSI electrolyte are shown in Figure S9, while the rate performance is represented in Figure 3 (also compared with that obtained in $NaPF_6$-PC). Finally, the dQ/dV plots upon charging and discharging are given in Figure 4. The comparison shows that only the charge plateau at 4.2 V is sensitive towards the type of used electrolyte, while the other electrochemical peaks at 3.2 and 3.6 V appear to be unchanged. When using the IL-based electrolyte, the length of the plateau at 4.2 V shortens in comparison with that measured in the $NaPF_6$-PC electrolyte irrespective of the operating temperature. As a result, NM-16 delivers after the first charging in IL a lower specific capacity at both 20 °C and 40 °C: 95 *versus* 137 mAh/g at 20 °C and 135 *versus* 164 mAh/g at 40 °C (Figs. S8
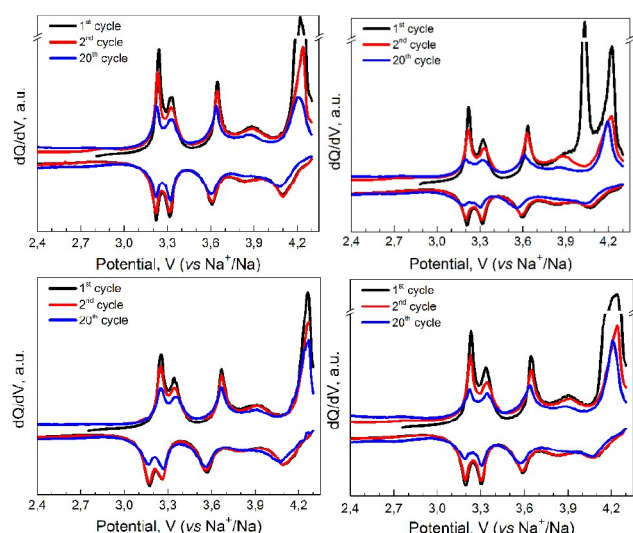

Figure 4. dQ/dV curves upon charging/discharging with 0.1 C-rate of NM-16 electrodes cycled in $NaPF_6$-PC electrolyte at 20 °C (top, left) and 40 °C (top, right), as well as in NaFSI-Pyr_{14}FSI electrolyte at 20 °C (bottom, left) and 40 °C (bottom, right). To make clear, the dQ/dV derivatives are shown only down to 2.4 V.

and S9). It is of importance that the charge capacities determined in IL electrolyte are still higher than the expected one for extracting 1/3 of Na^+ out of $P3$-$Na_{2/3}Ni_{1/3}Mg_{1/6}Mn_{1/2}O_2$ due to the blocking effect of Mg^{2+}. In comparison with the charge capacity, the discharging curve does not undergo any significant changes and the first discharge capacity is slightly lower than that obtained in $NaPF_6$-PC electrolyte. This means that the first irreversible capacity is limited in the IL electrolyte. Indeed, at 20 °C the irreversible capacity is 5.3 mAh/g in IL versus 39.4 mAh/g in $NaPF_6$-PC; while at 40 °C these values are 36.0 versus 53.9 mAh/g. It is noticeable that the first irreversible capacity remains low in IL electrolyte even at the function of NM-16 at temperature of 60 °C: 49 mAhg (Figure S10). The reduction in the first irreversible capacity reveals that IL electrolyte suppresses kinetically limited reaction at 4.2 V at elevated temperature.

Furthermore, the difference between these two kinds of electrolytes is also illustrated by the rate capability measured at 20 and 40 °C (Figure 3). In the IL, the rate performance at elevated temperature (i.e. 40 °C) is better than that at 20 °C in contrast to the $NaPF_6$-PC electrolyte. The improved rate performance at elevated temperature is also established with $NaFePO_4$, $Na_3V_2(PO_4)_3$ and layered oxides electrodes, when they are cycling in IL electrolytes.[35,39,36] This is usually related with the enhanced thermal stability of IL electrolytes than the carbonate-based one. In the case of NM-16, the cathode-electrolyte inter-phase looks like insensitive towards the operating temperature (20 and 40 °C, see Table 3 and the next discussions) and the wetting of oxide by the IL electrolyte at 40 °C can also be taken into account. (It is worth mentioning that the experiments in IL are represented only up to 40 cycles due to the corrosion of Al collector by NaFSI.[43])

2.3. Ex Situ Structural Characterization of Electrodes

In order to understand the changes occurring in the electrodes cycled in both the carbonate- and the IL-based electrolytes, ex-situ XRD, TEM and EPR analyses were performed. The investigation was carried out on NM-16 electrodes cycled at 20 and 40 °C in $NaFSI$-$Pyr_{14}FSI$ between 4.3 and 2.0 V for 80 cycles and recovered from cells in the desodiated (4.3 V) and sodiated state (2.0 V). For comparison, the NM-16 electrodes cycled in the $NaPF_6$-PC electrolyte were also studied.

Figure 5 shows the XRD patterns of NM-16 electrodes as originally made and after desodiation (up to 4.3 V) and sodiation (down to 2 V) at 20 °C and 40 °C. For the NM-16 electrode charging in $NaFSI$-$Pyr_{14}FSI$ to 4.3 V, the XRD pattern is indexed in a $P3$-type of structural model. The a-parameter
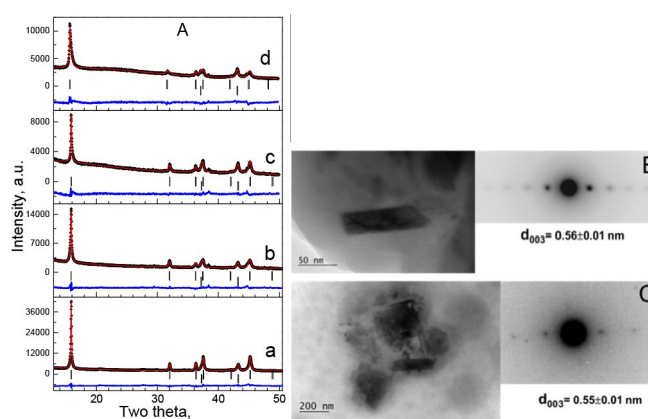

Figure 5. XRD patterns (A) of pristine NM-16 electrodes (a) and after charge to 4.3 V in IL-based electrolyte at 20 °C (b), discharging at 2.0 V cycled in the IL-based electrolyte at 20 °C (c) and 40 °C (d). (right) Bright field micrographs and SAED of a discharged at 40 °C (B) and a charged at 20 °C (C) NM-16 electrode cycled in the IL-based electrolyte.

decreases, which reveals a contraction of the distance between TM ions inside the layers: from 2.889 to 2.876 Å (Table 1). This is consistent with an appearance of smaller highly oxidized Ni ions during the charging. In comparison with the a-parameter, the c-parameter increases, thus indicating an interlayer expansion: from 5.56 up to 5.64 Å expressed by d_{003} (Table 1). This is also related to an oxidation of the transition metal ions inside the layers leading to layers repulsion due to the reduction of the screening effect of Na^+. The restricted change in the interlayer space is also supported by the ex-situ TEM analyses, where d_{003} is simple calculated from SAED (Figure 5). The important finding here is the relatively small interlayer expansion during the Na^+ extraction. This is in contrast with the unsubstituted oxide $P3$-$Na_{2/3}Ni_{1/2}Mn_{1/2}O_2$, where an enormous high interlayer expansion (more than 20%) is established during Na^+ extraction in the $NaPF_6$-based electrolyte: from 5.6 to 7.0 Å.[24] The large interlayer expansion is supposed to be a consequence of the insertion of solvent molecules or salt ions from electrolyte into the interlayer space released by Na^+.[24] The same phenomenon has been established for $P3$-$Na_{0.5}[Ni_{0.25}Mn_{0.75}]O_2$, where the intercalated counter-anion ClO_4^- from electrolyte salt contributes to the activation of the oxygen redox reaction.[20] Therefore, the possible electrolyte molecule insertion could be related to the kinetically limited process taking place above 4.0 V (Figure 4).

When Mg^{2+} substitutes the Ni ions in the layered oxide, it appears that the process of electrolyte molecule insertion is restricted. Supporting this suggestion, it is worth mentioning that Mg substituted oxide with composition $Na_{2/3}Ni_{1/4}Mg_{1/12}Mn_{2/3}O_2$ and $P3$-type structure has been shown to be stable even after soaking in water, i.e. the water molecules are not inserted into the interlayer space of $P3$-$Na_{2/3}Ni_{1/4}Mg_{1/12}Mn_{2/3}O_2$.[44] Therefore, the Mg^{2+} ions enhance the rigidity of the layered structure towards electrolyte and water molecules insertion, resulting in a suppression of the kinetically limited electrochemical reaction at 4.2 V. In addition, the role of Mg^{2+}

Table 3. Surface composition for soaked and cycled at 20 and 40 °C NM-16 electrodes in the IL electrolyte.

Sample	Na/S	F/S	O/S	Na/S
soaked NM-16	2.10	2.14	3.45	1.10
NM-16 cycled at 20 °C	0.65	1.35	1.87	0.97
NM-16 cycled at 40 °C	0.59	0.97	1.81	0.95

Batteries & Supercaps

Articles
doi.org/10.1002/batt.202000137

**Chemistry
Europe**
European Chemical
Societies Publishing

is to initiate a new type of reaction, which is occurring above 4.0 V and it is reversible.

The EPR spectroscopy allows probing the oxidation state and distribution of transition metal ions inside the layers during charging and discharging. The oxidation of paramagnetic Ni^{2+} ($S=1$) and Ni^{3+} ($S=1/2$) ions yields Ni^{4+} ions, which are diamagnetic ($S=0$). As a result, in case of the charged NM-16, one could expect the observation of an EPR signal with a g-factor that is slightly dependent on the temperature as in the case of diamagnetic Mg^{2+} ions (See Figure S2). Contrary to the expectation, the g-factor displays strong temperature dependence: on cooling down from 300 to 140 K, the g-factor decreases, followed by an abrupt increase below 140 K. The abrupt change in the g-factor is concomitant with a corresponding change in the EPR line width (Figure 6). This concerted change in the g-factor and EPR line width can be related to a cationic redistribution process causing an occurrence of Ni^{2+} in the desodiated layers. The location of Ni^{2+} ions inside two adjacent layers provokes a development of antiferromagnetic interactions between them due to the formation of 180° configuration via O.[45,46] The 180° interlayer interactions between nickel ions are stronger in magnitude than the exchange interactions between nickel and manganese ions inside the layers, which are coupled by 90° via O.[47,48] This is the main reason for the observation of 180° Ni–O–Ni configurations in magnetically concentrated $P3$-$Na_{2/3}Ni_{1/3}Mg_{1/6}Mn_{1/2}O_2$ by EPR. It is worth mentioning that magnetically coupled Ni^{2+} ions

with 180° interactions are also found out to be EPR active in Ni-rich lithium oxides $Li_{1-x}Ni_{1+x}O_2$ (at 210 K[47,48]) and $LiNi_{1/2}Mn_{1/2}O_2$ (at 130 K[45]). In general, for the lithium oxides the Ni^{2+}-Li^+ exchange reaction between layers is a common phenomenon due to the close values of ionic radii of Li^+ and Ni^{2+} ions.[49] In sodium oxides studied by us, the Ni ions from the transition metal layers become moveable in the case, when the bigger Na^+ ions from the interlayer slab are being extracted. Furthermore, the transfer of Ni^{2+} in the desodiated interlayer slab will block the insertion of the electrolyte molecules into the oxide, thus supporting *ex-situ* XRD and TEM data on rigidity of the layered structure of the Mg-substituted oxide (Figure 5). This is the main difference between Mg-containing and Mg-free oxides during charging up to 4.3 V. It deserves to remind the fact that by EPR only the transfer of Ni^{2+} ions is detected, while the possible migration of Mg^{2+} ions between layers can only be guessed due to the close values of ionic radii of Ni^{2+} and Mg^{2+} ions. Taking into account the higher polarizing power of Ni^{2+} than that of Mg^{2+}, one could suppose that there is a competition between Ni and Mg mobility, in which the Mg-mobility is the more favorable process. The migration of Mg^{2+} ions during Na intercalation is also being observed for Mg-substituted sodium manganese oxide, $P3$-$Na_{2/3}Mg_{1/3}Mn_{2/3}O_2$, which does not contain nickel ions.[14] Based on EPR spectroscopy, Ni^{2+} ions are detected in the interlayer space of cycled NM-16. Since this phenomenon is specific for cycled NM-16, one can conclude that Mg^{2+} ions initiate the Ni^{2+} mobility too. The cationic redistribution during cycling can be considered as a factor giving rise to an oxygen redox activity. It is noticeable that the formation of specific local environments around oxygen atoms in Li-excess oxides has been correlated with a liability of oxygen electrons that can be more easily extracted and they participate in the practical capacity of cathodes.[19]

After discharging down to 2.0 V, the $P3$-layered structure remains stable and the lattice parameters a and c are recovered (Figure 6, Table 1). The EPR spectrum is also recovered (Figure 6). Indeed, the g-factor of the discharged electrode is close to that of the pristine oxide, which is revealing a recovering of the Ni–Mn spin system after electrode discharging down to 2.0 V. On the other hand, this demonstrates a disappearance of Ni^{2+} from the interlayer space in the discharged electrode. This is an EPR evidence for reversible Ni^{2+}-Mg^{2+} cationic migration between layers during Na^+ intercalation. Further proof for cationic migration is the EPR line width (Figure 6): the comparison shows that the EPR line width of discharged NM-16 is slightly higher than that of the pristine NM-16. This implies, most probably, that there occurs a creation of some defects in layer stacking of the cycled oxide.

The replacement of IL by carbonate-based electrolyte causes more significant changes in the structure of electrodes. After discharging down to 2.0 V, both a and c lattice parameters show a tendency to be higher than that of the pristine values (Table 1). Although the g-factor seems unchanged, the EPR line width is larger than that of the pristine oxide, as well as of the oxide discharged down to 2.0 V in the NaFSI-Pyr_{14}FSI electrolyte (Figure 6). These results reveal that more defects in layer stacking are created, when the reaction
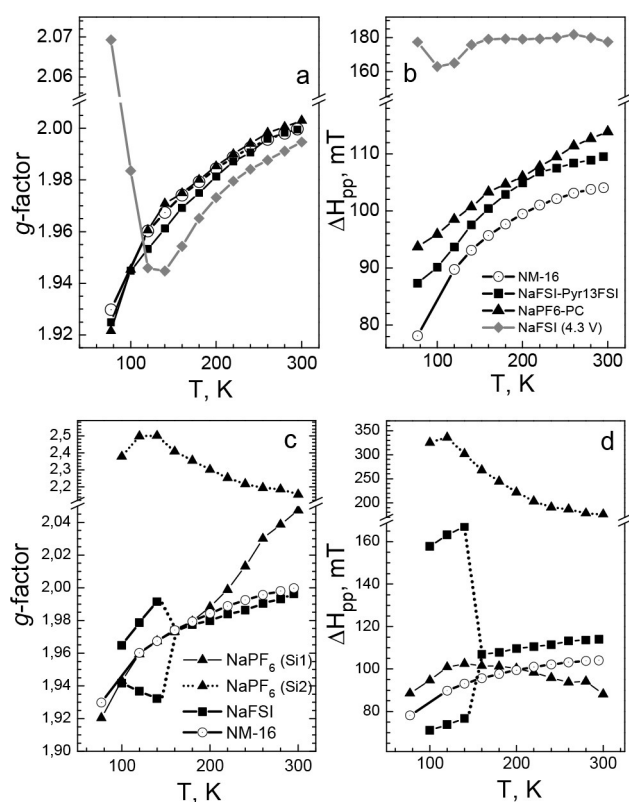

Figure 6. Temperature evolution of the g-factor (a, c) and EPR line width (ΔH_{pp}, b, d) for NM-16 electrode cycled in NaFSI-Pyr_{14}FSI with NaPF$_6$-PC electrolytes at 20 (a, b) and 40 °C (c, d).

Batteries & Supercaps

Articles
doi.org/10.1002/batt.202000137

Chemistry Europe
European Chemical
Societies Publishing

proceeds in the $NaPF_6$-PC electrolyte in comparison with that in the NaFSI-Pyr_{14}FSI electrolyte. On its turn, the accumulation of defects will give rise to the cycling stability of NM-16 electrode (Figure 3).

The operating temperature is the next parameter that provokes the structure change of the electrode. Although the lattice parameters of NM-16 cycled in NaFSI-Pyr_{14}FSI and $NaPF_6$-PC electrolytes are not sensitive with respect to the operating temperature (Table 1), the EPR spectrum undergoes a strong variation, when the reaction proceeds at elevated temperature (Figure 6). Between 300 and 160 K, the g-factor and the EPR line width for NM-16 cycled in NaFSI-Pyr_{14}FSI at 40°C are close to that of the pristine composition, whereas below 160 K the signal is split into two components (Figure 6). One of them possesses a higher g-value and a larger EPR line width than that of the pristine oxide, while the other one is characterized by a slightly lower g-value and EPR line width. Based on the EPR spectrum of charged NM-16, one can assign the broader signal to Ni ions that remain blocked in the interlayer space during the discharging, while the narrower signal originates from the Ni—Mn spin system that is reversibly reduced during Na^+ intercalation. On this level of the study, it is not clear why some of Ni ions remained in the interlayer slab, while others are reversibly moveable. However, the important finding is the amount of Ni ions, which are much more than those observed at 20°C. (It deserves to remind that the sensitivity of XRD towards Ni^{2+} in the interlayer space is lower than that of the EPR,[46] as a result of which the lattice parameters of NM-16 cycled in NaFSI-Pyr_{14}FSI and $NaPF_6$-PC electrolytes are close). This implies that the transfer of nickel ions from the transition metal layers to the interlayer slab is facilitated at elevated temperature. The acceleration of the ionic transfer will, furthermore, contribute to the rate capability of NM-16 at elevated temperature (Figure 3).

The effect of the electrolyte composition on the rate capability is further examined by EPR (Figure 6). For the oxide cycled in $NaPF_6$-PC at 40°C, the signal consists of two overlapping lines even at room temperature (i.e. at 290 K, Figure 6). The first signal is broader and exhibits a g-value within the range of 2.2 and 2.5. This signal comes from Ni ions in the interlayer slab. The second signal displays EPR parameters that do not deviate much from those typical of Ni—Mn spin system in NM-16. The EPR data show that, in addition of the Ni—Mn spin system, the significant amount of Ni ions in the interlayer slab is blocked for the oxide cycled in $NaPF_6$-PC at 40°C. This coincides with a higher irreversible capacity, observed after the first cycle (Figure 3). The comparison between the effects of the operating temperature and the electrolyte composition indicates that the reaction of the ionic transfer between layers proceeds more easily at elevated temperature and in the $NaPF_6$-PC electrolyte. In addition to the cationic redistribution, one can take into account the low thermal stability of the carbonate-based electrolyte.[40] These are the conditions, under which the oxide has the worse rate capability (Figure 3). Therefore, one can conclude that the NM-16 displays better electrochemical properties in the NaFSI-Pyr_{14}FSI electrolyte, especially at elevated temperatures where

the thermal stability, conductivity and the viscosity of IL are improved.

The advantage of NaFSI-Pyr_{14}FSI over $NaPF_6$-PC is also demonstrated by thermal stability of NM-16 electrodes (Figure 7). For the sake of comparison, the thermal decomposition of the pristine electrode is also given in the same Figure. The pristine electrode undergoes decomposition above 300°C due to the combustion of carbon additives.[50] In comparison with the pristine electrode, both the charged and discharged electrodes in the IL electrolyte are stable up to 300°C, while in case of the electrode cycled in $NaPF_6$-PC there is a continuous mass loss after 100°C. This reveals an improved thermal stability of the electrode cycled in the IL electrolyte than that in $NaPF_6$-PC. It is worth mentioning that NaFSI salt is less stable than the $NaPF_6$ salt presenting decomposition temperatures of 300°C and 400°C, respectively.[43] This implies that the thermal decomposition of cycled electrodes is dominated to greater extent by the cathode-electrolyte inter-phase, rather not by electrolyte salt adsorption on electrode surface. Supporting this supposition, the thermal decomposition of electrodes includes mainly the release of CO_2 irrespective of the kind of the used electrolyte and state of charging and discharging (Figure 7).

2.4. Ex Situ Surface Characterization of $P3$-$Na_{2/3}Ni_{1/3}Mg_{1/6}Mn_{1/2}O_2$

The surface chemical composition of the cycled electrodes has been assessed by XPS spectroscopy. An important parameter of this surface-sensitive method is the analysis in depth, which depends strongly on the inelastic mean free path (λ) of the photoemitted electrons. The XPS signal decays exponentially in the depth below the surface as the uppermost surface layer having a thickness of λ gives around 60% contribution to the total signal. 95% of this signal comes from the surface layer having a thickness of 3λ, which is assumed to be the analysis depth of XPS. The mean free paths of photoemitted electrons depend on their kinetic energies such as for Li 1s- or Na 2s-
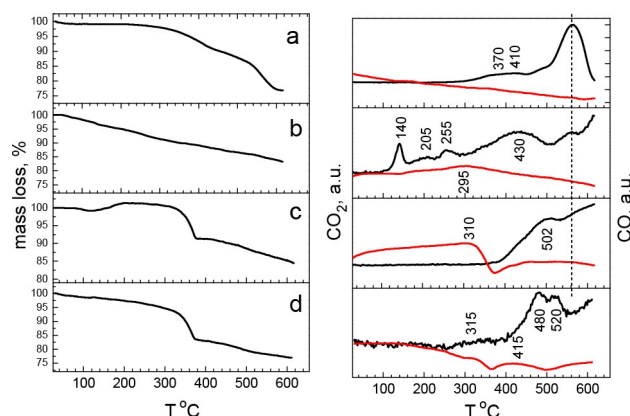

Figure 7. Thermo-gravimetric (left), CO_2 (right, black) and CO (right, red) curves of NM-16 electrodes: pristine NM-16 (a); discharged NM-16 cycled in NaPF6-PC (b); discharged NM-16 cycled in the IL electrolyte (c); charged NM-16 cycled in the IL electrolyte (d).

electrons, λ is close to 2 nm and therefore the analysis in depth is about 6 nm, whereas for Na 1s electrons (with significantly lower kinetic energy) λ is about 1 nm and the corresponding depth of analysis is about 3 nm. This illustrates the surface-layer thickness that is examined by XPS measuring the photo-emitted electrons from different core-levels.

Figure 8 displays the XPS spectra of cycled electrodes in the energy region of Na 1s, Na 2s, F 1s, S 2p, O 1s and N 1s. The same figure gives, in addition, the corresponding XPS spectra for the NM-16 electrode, which is soaked in the IL electrolyte for 24 hours prior to the cell cycling. Under these conditions, the OCV remains constant, thus indicating the lack of redox interaction between electrode and electrolyte (Figure S11, SI). The peaks identification is based on previous reference data for NaF, PVdF, FSI$^-$ and Pyr$_{14}$.[51,52,53]

In the Na1s and Na2 s regions, only symmetric peaks are observed independently of the cycling or the operating temperature (Figure 8). These peaks can be assigned to Na atoms in NaF.[54] In agreement with this assignment, the F 1s spectrum shows a peak at 684 eV typical of F atoms in NaF.[55,56] As in the case of Na 1s and Na 2s, the F 1s peak at 684 eV is independent of cycling conditions. Taking into account the relative sensitivity factors of Na 1s and F 1s photo-emitted electrons, the ratio between the concentrations of Na and F atoms in the studied surface layer can be calculated. The result for the soaked electrode is F:Na = 37:63 at%, which is different from the stoichiometric ratio of 1:1 for NaF. Therefore, a contribution to the Na 1s signal by the electrode (comprising NM-16 and the PvDF binder) should be assumed. This is further evidenced by the presence of a second F 1s peak at higher binding energies of 687.7 eV, which is a fingerprint for the PvDF.[57] These considerations indicate that before the electrochemical reaction the surface of NM-16 is covered by a NaF layer with a thickness less than the analysis depth for Na 1s, which is 3 λ = 3 nm (see above). The total relative amount of Na is 63 at.% from which 37 at.% belong to Na of NaF. Therefore, 60% of the total Na 1s-signal comes from the NaF surface layer. It follows from our considerations at the beginning of this section that the thickness of this layer is near to 1 λ = 1 nm.

The appearance of surface NaF can be explained in terms of a surface interaction occurring during the electrode fabrication comprising NM-16 and the PvDF binder. The NaF layer undergoes significant changes during the electrode cycling at 20 °C and 40 °C: the F 1s peak at 684 eV decreases in intensity relative to the peak at 687.7 eV due to the PvDF binder (Figure 8b, c). This could be explained by the formation of a mixed layer of PvDF and NaF and/or by the deposition of additionally surface compounds. This new layer can further shield the XPS signal from the underlying layers. A confirmation of the existence of a new surface layer for the cycled electrodes could be found in the spectral region of low binding-energies, which does not display any signals due to Ni 3p, Mg 2p and Mn 3p (Figure 8b, c). This is an indication that the surface film becomes thicker during the electrode cycling. Its thickness should be greater than the analysis depth in this spectral region (i.e. more than 6 nm).

The chemical characterization of the formed surface layer is based on the changes in the photoelectron lines of the soaked electrode as a result of the cycling. The comparison between soaked and cycled electrodes is shown in Figure 8, where it can be seen that, except for the F 1s peaks, significant changes also occur in the S 2p, N 1s and O 1s regions.

The S 2p energy region of soaked and cycled electrodes are dominated by two components which result from spin-orbit S 2p$_{3/2}$ and S 2p$_{1/2}$ doublet (Figure 8). These components originate from S atoms included in FSI$^-$ counter-ions.[54,57] The detection of FSI$^-$ points out that the electrolyte salt is adsorbed without decomposition on the electrode surface, this adsorp-
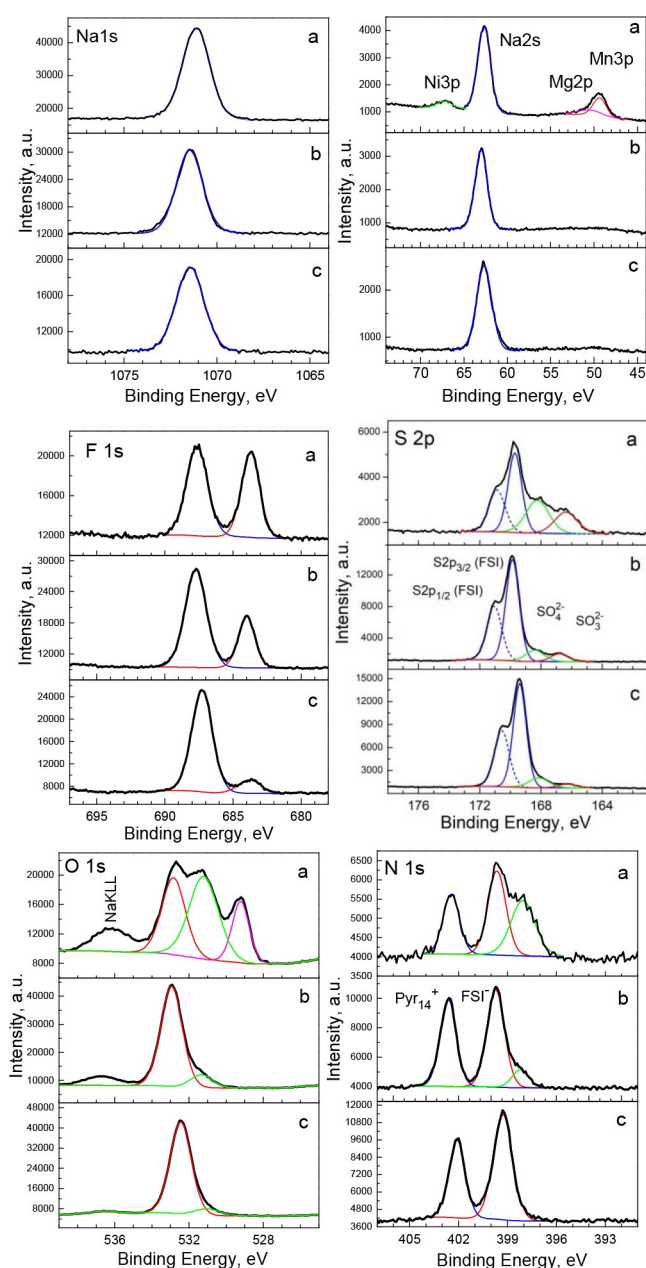
Figure 8. XPS spectra in the energy region of Na 1s, Na 2s, F 1s, S 2p, O 1s and N 1s for soaked (a) and cycled NM-16 electrodes at 20 °C (b) and 40 °C (c) in the IL electrolyte.

tion proceeds before the electrochemical reaction. In addition, two less intensive peaks at around 166.5 and 168.5 eV are superimposed on the peak due to FSI⁻. These peaks are too broad, which prevents to resolve the spin-orbit doublets. However, the two peaks can be attributed to S atoms in sulfites/sulfonyls and sulfates, respectively.[54,57] The origin of sulfur-containing products is associated with a decomposition of FSI⁻ counter-anion.[51] These sulfur-containing decomposed products can serve as a witnessed on the participation of the IL electrolyte in the surface film growth after soaking and electrode cycling at room and elevated temperature (Figure 8). It is well accepted that NaFSI is decomposed yielding $N(SO_2)_2^{3-}$ and NaF.[44]

The formation of sulfates is also detected by the XPS spectra in the energy region of O 1s (Figure 8). The peak typical for O atoms in Na_2SO_4 appears at around 531.5 eV.[58] It is worth to recall that Na atoms in NaF and Na_2SO_4 exhibit close binding energies. The O 1s spectrum of the soaked electrode displays additional peaks with binding energies corresponding to the lattice oxygen (i.e. 529.2 eV) and FSI⁻ counter ion (i.e. 533 eV). This indicates that the surface film on the soaked NM-16 is either thinner or more inhomogeneous than that for cycled electrode. It was shown above that most likely this layer is much thinner.

The XPS spectra in the N 1s region provide further evidences for the presence of decomposed electrolyte products. The spectra of all the samples can be deconvoluted at least of three components; two of them correspond to electrolyte ions Pyr_{14}^+ and FSI⁻. The last component at about 398 eV can be attributed to the nitride products, whose concentration decreases compared to that of FSI⁻. This behavior is similar to the concentration decrease of sulfites/sulfonyls and sulfates from FSI⁻ decomposition products during the cycling (Figure 8).

In general, the electrodes cycled at 20 °C and 40 °C display similar surface compositions and thickness of the surface film (Table 3). The composition of the surface film is dominated by the adsorption of the electrolyte ions. The electrolyte-electrode interaction leading to the deposition of sulfates, sulfites/sulfonyls, nitrides, NaF products, takes place in a low extent. This suggests a low reactivity of the IL electrolyte towards the layered oxide. In comparison with IL electrolyte, $NaPF_6$-based electrolyte has been shown to be highly reactive, resulting in the formation of interface rich on inorganic and organic decomposition products.[55,56]

3. Conclusions

This work demonstrates firstly the elaboration of the electrode material with optimized structure and composition (i.e. $P3$-$Na_{2/3}Ni_{1/3}Mg_{1/6}Mn_{1/2}O_2$) which is designed to work at elevated temperatures.

Mg-substituted oxides, $Na_{2/3}Ni_{1/2-x}Mg_xMn_{1/2}O_2$, with a three layer stacking are obtained at 700 °C in a concentration range of $0 \leq x \leq 1/6$. In these oxides, Mg^{2+} ions substitute for Ni^{2+} ions, leading to a disruption of cationic ordering inside the

layer. At a threshold concentration of x = 1/6, the charge of Mg^{2+} is balanced by Ni^{3+} and Mn^{4+} ions. Between 1.5 and 4.3 V, $P3$-$Na_{2/3}Ni_{1/3}Mg_{1/6}Mn_{1/2}O_2$ is able to intercalate more than 1 mole of Na^+ (i.e. first charge capacity of 293 mAh/g) due to the redox activity of transition metal ions and lattice oxygen. In the limited potential window of 2.0–4.3 V, the specific capacity of $P3$-$Na_{2/3}Ni_{1/3}Mg_{1/6}Mn_{1/2}O_2$ is smaller, but it is still a consequence of the nickel and oxygen redox activities (i.e. 0.51 mole Na^+). The role of Mg^{2+} dopants in $P3$-$Na_{2/3}Ni_{1/2-x}Mg_xMn_{1/2}O_2$ is to increase the intercalation potential without reducing the intercalation capacity of the parent oxide.

The electrochemical behavior of the Mg-substituted oxide is related with the reaction of cationic redistribution, taking place at 4.2 V during the Na^+ extraction. The cationic redistribution is a reversible process and it includes a transfer of Mg^{2+} and Ni^{2+} ions from the TM layer to the Na^+-depleted interlayer slab. The cationic redistribution upon cycling could be supposed as a factor giving rise to an oxygen redox activity in Mg-substituted oxides. In addition, the presence of Mg^{2+} and Ni^{2+} ions in the interlayer slab is responsible for the suppression of the insertion of electrolyte molecule into oxides. The insertion of electrolyte molecule is a kinetic limited reaction, which takes place easily for the Mg-free oxide characterized with poorer rate capability than that of the Mg-substituted oxide.

The cationic redistribution process is intensified at elevated temperatures and in the $NaPF_6$-based electrolyte. Because of the lower thermal stability of $NaPF_6$-based electrolyte, the rate capability of NM-16 at elevated temperatures becomes worse in comparison with IL-based electrolyte. Moreover, the wettability of the active particles by the electrolyte solution depends on the electrolyte composition and the temperature. The best cycling stability and rate capability at elevated temperatures is observed for NM-16 cycled in IL-based electrolyte.

The advantages of using ILs as electrolytes are related to the first irreversible capacity and the thermal stability of cycled electrodes. In the IL electrolyte, the first irreversible capacity is reduced irrespective of the operating temperature. Charged and discharged electrodes cycled in the IL electrolyte are stable up to 300 °C, while there is a continuous mass loss above 100 °C for the electrodes working in the $NaPF_6$-based electrolyte.

The IL electrolyte exhibits a low surface reactivity towards layered oxide, which is not sensitive in respect of the operating temperature. The electrolyte-electrode interaction is dominated by the adsorption of the electrolyte ions. In addition, some surface reactions comprising of decomposed products such as sulfates, sulfites/sulfonyls, nitrides and NaF are also observed. The thickness of the surface film grows from 1 up to 6 nm upon cell cycling. The $NaPF_6$-PC electrolyte is more reactive in comparison with the IL-based electrolyte.

The extracted correlations between the structure, electrode surface, sodium capacity and rate capability of the Mg-substituted oxides at elevated temperature could be of significance for further understanding and controlling the electrochemical performance of materials with a colossal

intercalation capacity as next generation of electrodes in Li/Na ion batteries.

Experimental Section

Electrode Materials

Mg-substituted oxides, $P3$-$Na_{2/3}Ni_{1/2-x}Mg_xMn_{1/2}O_2$, were obtained via adapting the synthetic procedure used for the preparation of $P3$-$Na_{2/3}Ni_{1/2}Mn_{1/2}O_2$.[24,56,59] The synthetic procedure relies on the formation of homogeneous acetate precursors through freeze-drying of the corresponding acetate solutions (0.5 M) containing all metal ions. The nominal contents of Mg were 0.04, 0.08 and 0.16. The freeze-drying process was carried out using an Alpha-Crist Freeze-Dryer at $-20\,°C$ in vacuum. The freeze-dried acetates were decomposed at $400\,°C$ in O_2 atmosphere for 3 hours, followed by homogenization, palletization and annealing at $700\,°C$ in air for 24 hours. For the sake of convenience, $P3$-$Na_{2/3}Ni_{1/2-x}Mg_xMn_{1/2}O_2$ with nominal x=0.04, x=0.08 and x=0.16 will be denoted further by NM-04, NM-08 and NM-16, while the unsubstituted oxide $P3$-$Na_{2/3}Ni_{1/2}Mn_{1/2}O_2$ denoted by NNM.

Experimental Methods

Powder X-ray diffraction was performed using Bruker Advance D8 powder diffractometer applying the $CuK\alpha$ radiation in the 2θ range from $10°$ to $90°$. For ICP-OES measurements, a Prodigy 7 (Teledyne Labs) was used. The oxides were dissolved in a strongly acidic medium prior to the analysis. The TEM investigations were carried out on a JEOL 2100 microscope and a JEOL 2100 XEDS: Oxford Instruments, X–MAX^N 80T CCD Camera ORIUS 1000, 11 Mp, GATAN. The HRTEM analysis was quantified by the Digital Micrograph software. The X-ray photoelectron spectroscopy (XPS) was performed using AXIS Supra spectrometer (Kratos Analitycal Ltd.) with monochromatic $AlK\alpha$ source (1486.6 eV) and charge neutralization system. The photo-emitted electrons were separated, according to their kinetic energy, by a $180°$ -hemispherical analyzer having a total instrumental resolution of 0.54 eV (as it was measured by the FWHM of $Ag\ 3d_{5/2}$ line) at pass energy of 20 eV. The binding energies (BE) were determined with an accuracy of ± 0.05 eV. The curve profiles of the XPS spectra were analyzed using a symmetrical Gaussian-Lorentzian curve fitting after Shirley's type subtraction of the background. The commercial data-processing software of Kratos Analytical Ltd. was employed for the calculation of elemental concentrations in atomic %. The EPR spectra were recorded on a Bruker EMX^{plus} spectrometer within the temperature range of 100–400 K. The thermal properties charging and discharging electrodes were monitored by a simultaneous TG/DTA/mass spectrometry analysis using LABSYS™ Evo apparatus (SETARAM) using a heating rate of $10\,°C\ min^{-1}$ under nitrogen.

Electrochemical Characterization

The $P3$-$Na_{2/3}Ni_{1/2-x}Mg_xMn_{1/2}O_2$ electrodes were prepared by mixing the active material with carbon black (Super C65, IMERYS) and polyvinylidene fluoride (PVDF; Solef 6020, Solvay Polymer Specialties) dissolved in N-methyl-2-pyrrolidone (NMP, 10% solution), at a dry weight ratio of 85:10:5. After drying at $60\,°C$ overnight, disk electrodes with a diameter of 12 mm were cut out, pressed and additionally dried at $120\,°C$ under vacuum overnight. Three-electrode, Swagelok-type cells were mounted in a glovebox (MBraun, 200BECO, H_2O, and O_2 content <0.1 ppm) under Ar atmosphere. Sodium metal, serving as reference and counter electrode, was cut out of sodium sticks (Acros Organics, 99.8%),

pressed, and punched on the current collectors. Two types of electrolyte solutions were applied: (i) carbonate-based electrolyte consisting of 1 M $NaPF_6$ (Kishida Chemicals, $\geq 99\%$) in PC (UBE, Japan), and (ii) the IL-based electrolyte comprising 1 M NaFSI (PROVISCO) in $Pyr_{14}FSI$ (synthesized in-house) at the 1:9 molar ratio. The water content in IL-based electrolyte was lower than 8 ppm in view of checked Karl Fischer titration (Mettler-Toledo). A Whatman GF/D glass microfiber layer was used as separator and soaked with 140 µl of electrolyte. The cell testing was carried out using a Maccor battery cycler (Series 4000) in galvanostatic mode. Each electrochemical experiment was repeated at least twice, showing a rather high reproducibility. The *ex-situ* TEM, XPS and EPR experiments were carried out on the electrodes recovered from cells, stopped at selected potentials (i.e., states of charging or discharging). The electrochemical cells were disassembled inside the glove-box, and the recovered electrodes were subjected to a washing step with dimethyl carbonate (DMC) to eliminate electrolyte residues.

Conflict of Interest

The authors declare no conflict of interest.

[1] a) M. S. Whittingham, *Chem. Rev.* **2004**, *104*, 4271–4302; b) N. Yabuuchi, K. Kubota, M. Dahbi, S. Komaba, *Chem. Rev.* **2014**, *114*, 23, 11636–11682; c) J.-Y. Hwang, S.-T. Myung, Y.-K. Sun, *Chem. Soc. Rev.* **2017**, *46*, 3529–3614.

[2] J. Wang, X. He, E. Paillard, N. Laszczynski, J. Li, S. Passerini, *Adv. Energy Mater.* **2016**, *6*, 1600906.

[3] D. Andre, S.-J. Kim, P. Lamp, S. F. Lux, F. Maglia, O. Paschos, B. Stiaszny, *J. Mater. Chem. A* **2015**, *3*, 6709–6732.

[4] R. Stoyanova, A.-L. Barra, M. Yoncheva, E. Kuzmanova, E. Zhecheva, *Dalton Trans.* **2011**, *40*, 9106–9115.

[5] C. Pouillerie, F. Perton, P. Biensan, J. P. Peres, M. Broussely, C. Delmas, *J. Power Sources* **2001**, *96*, 293–302.

[6] M. Mladenov, R. Stoyanova, E. Zhecheva, S. Vassilev, *Electrochem. Commun.* **2001**, *3*, 410–416.

[7] H. Li, P. Zhou, F. Liu, H. Li, F. Cheng, J. Chen, *Chem. Sci.* **2019**, *10*, 1374–1379.

[8] Q. Liu, K. Du, H. Guo, Z.-D. Peng, Y.-B. Cao, G.-R. Hu, *Electrochim. Acta.* **2013**, *90*, 350–357.

[9] G. T. K. Fey, J. G. Chen, V. Subramanian, *J. Power Sources.* **2003**, *119–121*, 658–663.

[10] N. Yabuuchi, R. Hara, K. Kubota, J. Paulsen, S. Kumakura, S. Komaba, *J. Mater. Chem. A* **2014**, *2*, 16851–16855.

[11] D. Buchholz, C. Vaalma, L. G. Chagas, S. Passerini, *J. Power Sources.* **2015**, *282*, 581–585.

[12] Z.-Y. Li, R. Gao, J. Zhang, X. Zhang, Z. Hu, X. Liu, *J. Mater. Chem. A* **2016**, *4*, 3453–3461.

[13] N. Tapia-Ruiz, W. M. Dose, N. Sharma, H. Chen, J. Heath, J. W. Somerville, U. Maitra, M. Saiful Islam, P. G. Bruce, *Energy Environ. Sci.* **2018**, *11*, 1470–1479.

[14] B. Song, E. Hu, J. Liu, Y. Zhang, X.-Q. Yang, J. Nanda, A. Huq, K. Page, *J. Mater. Chem. A* **2019**, *7*, 1491–1498.

[15] H. Koga, L. Croguennec, M. Ménétrier, P. Mannessiez, F. Weill, C. Delmas, *J. Power Sources* **2013**, *236*, 250–258.

[16] C. Delmas, C. Fouassier, P. Hagenmuller, *Physica B+C* **1980**, *99*, 81–85.

[17] E. McCalla, A. M. Abakumov, M. Saubanère, D. Foix, E. J. Berg, G. Rousse, M.-L. Doublet, D. Gonbeau, P. Novák, G. Van Tendeloo, R. Dominko, J.-M. Tarascon, *Science* **2015**, *30*, 1516–1521.

[18] K. Luo, M. R. Roberts, R. Hao, N. Guerrini, D. M. Pickup, Y. S. Liu, K. Edström, J. Guo, A. V. Chadwick, L. C. Duda, P. G. Bruce, *Nat. Chem.* **2016**, *8*, 684–691.

[19] D. H. Seo, J. Lee, A. Urban, R. Malik, S. Kang, G. Ceder, *Nat. Chem.* **2016**, *8*, 692–697.

[20] Q. Li, Y. Qiao, S. Guo, K. Jiang, Q. Li, J. Wu, H. Zhou, *Joule* **2018**, *2*, 1134–1145.

[21] E. J. Kim, L. A. Ma, L. C. Duda, D. M. Pickup, A. V. Chadwick, R. Younesi, J. T. S. Irvine, A. R. Armstrong, *ACS Appl. Energy Mater.* **2020**, *3*, 184–191.

[22] G. Singh, N. Tapia-Ruiz, J. M. Lopez del Amo, U. Maitra, J. W. Somerville, A. R. Armstrong, J. Martinez de Ilarduya, T. Rojo, P. G. Bruce, *Chem. Mater.* **2016**, *28*, 5087–5094.

[23] P.-F. Wang, Y. You, Y.-X. Yin, Y.-S. Wang, L. J. Wan, L. Gu, Y.-G. Guo, *Angew. Chem. Int. Ed.* **2016**, *55*, 7445–7449; *Angew. Chem.* **2016**, *128*, 7571–7575.

[24] M. Kalapsazova, G. F. Ortiz, J. L. Tirado, O. Dolotko, E. Zhecheva, D. Nihtianova, L. Mihaylov, R. Stoyanova, *ChemPlusChem* **2015**, *80*, 1642–1656.

[25] M. Kalapsazova, H. Rasheev, E. Zhecheva, A. Tadjer, R. Stoyanova, *J. Phys. Chem. C* **2019**, *123*, 11508–11521.

[26] Z. Lu, R. A. Donaberger, J. Dahn, *Chem. Mater.* **2000**, *12*, 3583–3590.

[27] T. Risthaus, L. Chen, J. Wang, J. Li, D. Zhou, L. Zhang, D. Ning, X. Cao, X. Zhang, G. Schumacher, M. Winter, E. Paillard, J. Li, *Chem. Mater.* **2019**, *31*, 5376–5383.

[28] W. Zuo, J. Qiu, X. Liu, B. Zheng, Y. Zhao, J. Li, H. He, K. Zhou, Z. Xiao, Q. Li, G. F. Ortiz, Y. Yang, *Energy Storage Mater.* **2020**, *26*, 503–512.

[29] R. D. Shannon, *Acta Crystallogr.* **1976**, *A32*, 751–767.

[30] R. A. House, U. Maitra, L. Jin, J. G. Lozano, J. W. Somerville, N. H. Rees, A. J. Naylor, L. C. Duda, F. Massel, A. V. Chadwick, S. Ramos, D. M. Pickup, D. E. McNally, X. Lu, T. Schmitt, M. R. Roberts, P. G. Bruce, *Chem. Mater.* **2019**, *31*, 3293–3300.

[31] G. Ceder, Y.-M. Chiang, D. R. Sadoway, M. K. Aydinol, Y.-I. Jang, B. Huang, *Nature* **1998**, *392*, 694–696.

[32] R. Alcántara, P. Lavela, P. L. Relaño, J. L. Tirado, E. Zhecheva, R. Stoyanova, *Inorg. Chem.* **1998**, *37*, 264–269.

[33] M. C. López, G. F. Ortiz, P. Lavela, J. L. Tirado, R. Stoyanova, E. Zhecheva, *Chem. Mater.* **2013**, *25*, 4025–4035.

[34] J. Song, B. Xiao, Y. Lin, K. Xu, X. Li, *Adv. Energy Mater.* **2018**, *8*, 1703082.

[35] N. Wongittharom, C.-H. Wang, Y.-C. Wang, C.-H. Yang, J.-K. Chang, *ACS Appl. Mater. Interfaces* **2014**, *6*, 17564–17570.

[36] L. Mu, X. Feng, R. Kou, Y. Zhang, H. Guo, C. Tian, C.-J. Sun, X.-W. Du, D. Nordlund, H. L. Xin, F. Lin, *Adv. Energy Mater.* **2018**, *8*, 1801975.

[37] C.-M. Chu, C.-Y. Liu, Y.-Y. Wang, C.-C. Wan, C.-R. Yang, *J. Inst. Chem.* **2012**, *43*, 201–206.

[38] F. Wu, N. Zhu, Y. Bai, L. Liu, H. Zhou, C. Wu, *ACS Appl. Mater. Interfaces.* **2016**, *8*, 21381–21386.

[39] F. Wu, N. Zhu, Y. Bai, Y. Li, Z. Wang, Q. Ni, H. Wang, C. Wu, *Nano Energy* **2018**, *51*, 524–532.

[40] A. Ponrouch, D. Monti, A. Boschin, B. Steen, P. Johansson, M. R. Palacín, *J. Mater. Chem. A* **2015**, *3*, 22–42.

[41] A. Ponrouch, E. Marchante, M. Courty, J.-M. Tarascon, M. R. Palacín, *Energy Environ. Sci.* **2012**, *5*, 8572–8583.

[42] L. G. Chagas, S. Jeong, I. Hasa, S. Passerini, *ACS Appl. Mater. Interfaces* **2019**, *11*, 22278–22289.

[43] G. G. Eshetu, S. Grugeon, H. Kim, S. Jeong, L. Wu, G. Gachot, S. Laruelle, M. Armand, S. Passerini, *ChemSusChem.* **2016**, *9*, 462–471.

[44] Y.-N. Zhou, P.-F. Wang, X.-D. Zhang, L.-B. Huang, W.-P. Wang, Y.-X. Yin, S. Xu, Y.-G. Guo, *ACS Appl. Mater. Interfaces* **2019**, *11*, 24184–24191.

[45] M. Yoncheva, R. Stoyanova, E. Zhecheva, R. Alcántara, J. L. Tirado, *J. Alloys Compd.* **2009**, *475*, 96–101.

[46] N. A. Chernova, M. Ma, J. Xiao, M. S. Whittingham, J. Breger, C. P. Grey, *Chem. Mater.* **2007**, *19*, 4682–4693.

[47] R. Stoyanova, E. Zhecheva, S. Angelov, *Solid State Ionics* **1993**, *59*, 17–24.

[48] R. Stoyanova, E. Zhecheva, C. Friebel, *Solid State Ionics* **1994**, *73*, 1–7.

[49] E. Zhecheva, R. Stoyanova, *Solid State Ionics* **1993**, *66*, 143–149.

[50] B. Karamanova, A. Stoyanova, M. Shipochka, Ch. Girginov, R. Stoyanova, *J. Alloys Compd.* **2019**, *803*, 882–890.

[51] G. G. Eshetu, T. Diemant, M. Hekmatfar, S. Grugeon, R. J. Behm, S. Laruelle, M. Armand, S. Passerini, *Nano Energy* **2019**, *55*, 327–340.

[52] M. P. Do, N. Bucher, A. Nagasubramanian, I. Markovits, T. Bingbing, P. J. Fischer, K. P. Loh, F. E. Kühn, M. Srinivasan, *ACS Appl. Mater. Interfaces* **2019**, *11*, 23972–23981.

[53] L. Liu, X. Qi, S. Yin, Q. Zhang, X. Liu, L. Suo, H. Li, L. Chen, Y.-S. Hu, *ACS Energy Lett.* **2019**, *4*, 1650–1657.

[54] P.-Y. Brisson, H. Darmstadt, M. Fafard, A. Adnot, G. Servant, G. Soucy, *Carbon* **2006**, *44*, 1438–1447.

[55] M. Kalapsazova, R. Stoyanova, E. Zhecheva, G. Tyuliev, D. Nihtianova, *J. Mater. Chem. A* **2014**, *2*, 19383–19395.

[56] M. Kalapsazova, E. Zhecheva, G. Tyuliev, D. Nihtianova, L. Mihaylov, R. Stoyanova, *J. Phys. Chem. C* **2017**, *121*, 5931–5940.

[57] B. Erdem, R. A. Hunsicker, G. W. Simmons, E. D. Sudol, V. L. Dimonie, M. S. El-Aasser, *Langmuir* **2001**, *17*, 2664–2669.

[58] M. Fantauzzi, B. Elsener, D. Atzei, A. Rigoldi, A. Rossi, *RSC Adv.* **2015**, *5*, 75953–75963.

[59] M. Kalapsazova, E. Zhecheva, R. Stoyanova, *J. Solid State Electrochem.* **2014**, *18*, 2343–2350.